Journal of Computational Physics 231 (2012) 3389–3405

Contents lists available at SciVerse ScienceDirect

Journal of Computational Physics

journal homepage: www.elsevier.com/locate/jcp

Adapting the spectral vanishing viscosity method for large-eddy simulations in cylindrical configurations

K. Koal [a,*], J. Stiller [a], H.M. Blackburn [b]

[a] Institute of Fluid Mechanics, Technische Universität Dresden, 01062 Dresden, Germany
[b] Department of Mechanical and Aerospace Engineering, Monash University, Vic 3800, Australia

ARTICLE INFO

Article history:
Received 17 March 2011
Received in revised form 23 August 2011
Accepted 10 January 2012
Available online 20 January 2012

Keywords:
Large-eddy simulation
Spectral vanishing viscosity
Cylindrical coordinates
Spectral element method
Pipe flow

ABSTRACT

During the last decade the spectral vanishing viscosity (SVV) method has been adopted successfully for large-eddy-type simulations (LES) with high-order discretizations in both Cartesian and cylindrical coordinate systems. For the latter case, however, previous studies were confined to annular domains. In the present work, we examine the applicability of SVV in cylindrical coordinates to flows in which the axis region is included, within the setting of an exponentially convergent spectral element–Fourier discretization. In addition to the 'standard' SVV viscosity kernel, two modified kernels with enhanced stabilization in the axis region are considered. Three fluid flow examples are considered, including turbulent pipe flow. The results, on the one hand, show a surprisingly small influence of the SVV kernel, while on the other, they reveal the importance of spatial resolution in the axis region.

1. Introduction

The spectral vanishing viscosity (SVV) method was introduced by Tadmor [1] as a concept for stabilising Fourier spectral approximations of hyperbolic conservation laws. The main idea is to define a viscosity in spectral space that reaches a maximum at high wave numbers, but which vanishes for wave numbers below a resolution-dependent threshold. In this way stabilization is achieved through damping at fine length scales without degrading the convergence properties of the underlying discretization. Maday et al. [2] applied the SVV approach to Legendre spectral methods and introduced a smooth viscosity kernel, which was commonly adopted by subsequent researchers. Karamanos and Karniadakis [3] incorporated the method into a modal spectral element discretization of the incompressible Navier–Stokes equations and employed it for LES of turbulent channel flow. Xu and Pasquetti [4] adapted the SVV technique to the nodal spectral element method and investigated the importance of SVV parameters in applications to high-Reynolds number flows. Following these works, several researchers advocated SVV as a tool for LES, pointing out its conceptual simplicity and inherent spectral accuracy [5–10]. In particular this preservation of spectral convergence when the flow is well resolved renders SVV an attractive technique for LES when turbulent, transitional or laminar zones may co-exist.

Our motivation to explore the SVV technique emerged from studies of electromagnetic stirring of metal and semiconductor melts. Depending on the applied magnetic field, the flow may be turbulent only in a part of the container, or throughout the whole volume [11]. Although the degree of turbulence can be considerable, the flow tends to preserve a transitional character. Since most container configurations in stirring applications have rotational symmetry, we are interested particularly in an SVV formulation that is suitable for cylindrical coordinates. To our knowledge, Serre and co-workers are the only group to

* Corresponding author. Tel.: +49 351 46338092; fax: +49 351 46338087.
E-mail addresses: kristina.koal@tu-dresden.de (K. Koal), joerg.stiller@tu-dresden.de (J. Stiller), hugh.blackburn@eng.monash.edu.au (H.M. Blackburn).

0021-9991/$ - see front matter © 2012 Elsevier Inc. All rights reserved.
doi:10.1016/j.jcp.2012.01.014

have considered a corresponding approach to cylindrical coordinate configurations [8–10]. They incorporated the SVV technique into a Chebychev–Fourier spectral method and employed it to investigate turbulent rotor–stator flows including heat transfer. However, these studies were confined to annular domains and thus the results do not guarantee applicability to problems that include the axis. As will be shown below, the approach proposed in [8] is characterized by a loss of azimuthal SVV stabilization near the axis for any resolved mode and, as a result, non-physical accumulation of small scale structures may occur in this region.

The objective of this paper is to provide a validation of SVV for axisymmetric geometric configurations that may include the core region and to investigate possible remedies for near-axis accumulation. To that end, we first briefly recapitulate in Section 2 the principles of SVV in the setting of the one-dimensional diffusion equation. Following this, a detailed description is provided for development of SVV in a nodal spectral element–Fourier method for three-dimensional incompressible flows in cylindrical coordinates. We note that the underlying numerical method into which SVV was incorporated has previously demonstrated spectral convergence properties for direct numerical simulation (DNS) of flows in cylindrical coordinates where the axis is included [12]. In addition to the 'standard' SVV viscosity kernel, two modified kernels with enhanced stabilization in the axis region are introduced. In the following sections the SVV approach is applied to three different flow problems. As a first step, the spectral convergence of the method and the different kernels is verified in Section 3 by means of Kovasznay flow, as in the previous treatment [12]. Further assessment is based on LES of turbulent pipe flow at $Re_D = 10{,}000$ and the turbulent flow driven by a travelling magnetic field in a cylinder (Sections 4 and 5). In both these cases DNS serves as reference. In particular, we want to assess how far modifications of the SVV kernel or adaptions of the spatial resolution affect the flow characteristics near the axis. Finally, in Section 6, we summarize the main results and provide concluding remarks.

We note that while we have here focused on problems set in domains with a cylindrical geometry as well as coordinate system, the underlying discretization supports more general axisymmetric geometries. Additionally it will deal with three-dimensional Cartesian geometries which possess a homogeneous direction.

2. SVV spectral element–Fourier method

We consider the incompressible unsteady Navier–Stokes equations

$$\begin{aligned} &\partial_t \vec{u} + \vec{N}(\vec{u}) = -\rho^{-1}\nabla p + \nu\nabla^2\vec{u} + \rho^{-1}\vec{f}, \\ &\nabla\cdot\vec{u} = 0, \end{aligned} \tag{1}$$

where $\vec{u}$ represents the velocity, p the pressure, ρ and ν the density and kinematic viscosity of the fluid, and, if any exists, $\vec{f}$ the volume force. The nonlinear advection term $\vec{N}(\vec{u})$ can be composed in a number of ways which are equivalent for continua, but have different properties in discrete form. Here, the skew-symmetric form i.e. $\vec{N}(\vec{u}) = (\vec{u}\cdot\nabla\vec{u} + \nabla\cdot\vec{u}\vec{u})/2$ is employed for robustness.

The equations, expressed above in coordinate-free form, are subsequently written in cylindrical coordinate component form and discretized using a nodal spectral element method in the meridional (z,r) semi-plane and a Fourier spectral method in the azimuthal (φ) direction. Time integration is based on a second order velocity correction scheme with implicit treatment of diffusion. For details of the method and demonstration of its exponential convergence properties when implemented as a DNS technique we refer to [12].

2.1. Principles of the spectral vanishing viscosity method

To recap the principal ideas of the SVV method we start with the one-dimensional diffusion equation

$$\partial_t u = \nu\partial_x\partial_x u \quad \text{with} \quad x\in[0,2\pi]. \tag{2}$$

Solution periodicity is assumed at the limits of the domain. When the Fourier method is used for spatial discretization, the scalar u is decomposed in its complex Fourier modes $\hat{u}_k$ by

$$u(x,t) = \sum_{k=-\infty}^{\infty} \hat{u}_k(t)\exp(\mathrm{i}kx). \tag{3}$$

The exact forward and inverse Fourier transform require an infinite number of modes (cf. (3)), however, only a finite number of modes are retained in practice. Taking further into account the identity $\partial_x \exp(\mathrm{i}kx) = \mathrm{i}k\exp(\mathrm{i}kx)$, the discretized diffusion Eq. (2) can be written in Fourier space as

$$\partial_t \hat{u}_k = -\nu k^2 \hat{u}_k \quad \text{with} \quad -N \leqslant k \leqslant N, \tag{4}$$

where N and $-N$ denote the wave numbers of the highest considered mode and its complex-conjugate counterpart, respectively.

As mentioned in Section 1, the idea underlying SVV is to add a spectral viscosity term that reaches its maximum at the highest wave numbers, but vanishes for wave numbers below a resolution-dependent threshold. This is achieved by augmenting the diffusivity by the term $\varepsilon\widehat{Q}_k$ on the right hand side of (4):

$$\partial_t \hat{u}_k = -(\nu + \varepsilon\widehat{Q}_k)k^2\hat{u}_k \quad \text{with} \quad -N \leqslant k \leqslant N, \tag{5}$$

where ε is the maximum amplitude of the spectral viscosity and $\widehat{Q}_k$ is a modal shape function, referred to as the SVV kernel. The multiplication with $\widehat{Q}_k$ in spectral space corresponds to a convolution with Q in physical space. The SVV-stabilized diffusion equation thus reads in physical space

$$\partial_t u = \nu\partial_x\partial_x u + \varepsilon\partial_x(Q * \partial_x u), \tag{6}$$

with the convolution operator $*$.

Besides the above described restriction to a finite number of modes, the conjugate-symmetric property of the Fourier transform of real variables may be exploited, so that only the positive-k modes are required. Consequently, the modal SVV kernel $\widehat{Q}_k$ has only to be defined for positive wave numbers $0 \leqslant k \leqslant N$. Following Maday et al. [2] most authors have adopted the kernel given by

$$\widehat{Q}_k = \widehat{Q}(k) = \exp\left(-\frac{(N-k)^2}{(M-k)^2}\right), \quad M < k \leqslant N \tag{7}$$

and $\widehat{Q}_k = 0$ for $0 \leqslant k \leqslant M$, where M is the mode above which SVV is applied. Fig. 1 shows this kernel for $N = 31$ and various M.

When a nodal spectral element method is applied to the one-dimensional diffusion Eq. (2), the computational domain is split into elements and a polynomial expansion of the scalar u with a nodal function basis is employed within each element. Without loss of generality, we restrict the following derivation to the one-element case in the standard interval $\Omega^s = [-1,1]$. Furthermore, homogeneous boundary conditions — either Dirichlet or Neumann conditions — are presumed. Using the Lagrange cardinal functions h_i, $0 \leqslant i \leqslant P$ with the Gauß–Lobatto–Legendre (GLL) quadrature points x_i as an expansion basis, the projection of the scalar is given by

$$u(x,t) \approx \sum_{i=0}^{P} u_i(t)h_i(x), \tag{8}$$

where u_i is the scalar value at point x_i and P the polynomial order of the GLL-Lagrange basis. With $\dot{u}_i(t) = \mathrm{d}u_i(t)/\mathrm{d}t$ and $h_i'(x) = \mathrm{d}h_i(x)/\mathrm{d}x$ the Galerkin weak formulation of (2) then reads

$$\int_{\Omega^s}\left(\sum_{j=0}^{P}\dot{u}_j h_j\right)h_i\,\mathrm{d}\Omega = -\int_{\Omega^s}\left(\sum_{j=0}^{P}u_j h_j'\right)h_i'\,\mathrm{d}\Omega \tag{9}$$

or in matrix–vector notation

$$\sum_{j=0}^{P} M_{ij}\dot{u}_j = -\sum_{j=0}^{P} L_{ij}u_j, \tag{10}$$

where $\boldsymbol{M}$ and $\boldsymbol{L}$ are respectively the mass and stiffness (also referred to as Laplacian) matrices with

$$M_{ij} = \int_{\Omega^s} h_i h_j\,\mathrm{d}\Omega \quad \text{and} \quad L_{ij} = \int_{\Omega^s} h_i' h_j'\,\mathrm{d}\Omega \quad \text{for} \quad 0 \leqslant i,j \leqslant P. \tag{11}$$

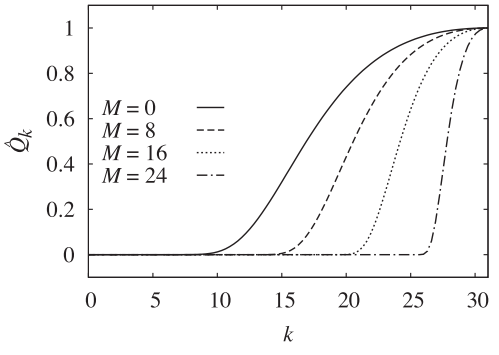

Fig. 1. Standard SVV kernel magnitude (7) as a function of wave number k.

Owing to use of GLL quadrature on the underlying nodal points, the mass matrix is diagonal, with the leading diagonal containing the quadrature weights ω_i and the stiffness matrix can be calculated by

$$L_{ij} = \sum_{l=0}^{P} \omega_l D_{li} D_{lj}, \tag{12}$$

where $\boldsymbol{D}$ is the GLL differentiation matrix in one-dimensional space. See [13] for more detail.

When incorporating SVV into the nodal spectral element method, two aspects must be considered. First, the GLL–Lagrange basis is not hierarchical, i.e. it does not have the property that smaller length scales are associated with increasing mode index. Projection into a suitable modal space is required before a spectrally vanishing viscosity can be adjoined to (9). This projection can be realized in various ways, e.g. by a mapping from nodal space to Legendre spectral space, or to the space of Jacobi-modal basis functions as employed for the *hp* form of the spectral element method (another hierarchical basis). In the present work we have restricted consideration to the Legendre polynomial space. The associated passage matrix $\boldsymbol{T}$ from physical to modal space is variously referred to as a discrete polynomial transform (DPT) matrix or a generalized Vandermonde matrix. See [14] Appendix A for details of how $\boldsymbol{T}$ may be computed. The second consideration is that the stiffness matrix $\boldsymbol{L}$ is symmetric, positive semi-definite, and it is required that SVV stabilization preserves these properties.

In order to satisfy both requirements, Xu and Pasquetti [4] proposed a symmetric form, where the SVV kernel is split by root extraction. Subsequently the kernel is applied to the standard differentiation matrix by counterposing it between the DPT matrix $\boldsymbol{T}$ and its inverse $\boldsymbol{T}^{-1}$. Thus, the modified differentiation matrix is given by

$$\boldsymbol{D}^{\mathrm{svv}} = \boldsymbol{T}^{-1} \mathrm{diag}\left(1 + \frac{\varepsilon}{\nu} \widehat{Q}_k\right)^{1/2} \boldsymbol{T}\boldsymbol{D}, \tag{13}$$

where $\widehat{Q}_k$ are the coefficients of the SVV kernel in (Legendre–) modal space which are defined in the same manner as presented in (7). The only difference is that, here, the polynomial order P replaces the highest Fourier wave number N.

As outlined above, the incorporation of SVV into the nodal spectral element is not quite so straight-forward as for the Fourier method, and has no simple direct counterpart in physical space equivalent to a global convolution. However, the principles are quite similar in each setting. In both cases — for the Fourier method as well as for the nodal spectral element method — augmentation of the diffusion equation with SVV involves only slight changes to the solution algorithm. In the first case, only the value νk^2 has to be modified for each mode, while in the second, the standard GLL differentiation matrix employed for diffusion operators has only to be manipulated once, during preprocessing. Consequently, the computational cost of either a direct solve or one PCG-type iteration step remains unchanged while additional damping is applied at small length scales, and this, together with the fact that the formal convergence properties may be unaltered, makes SVV an attractive method.

2.2. SVV for three-dimensional flow equations in cylindrical coordinates

As seen above, SVV influences exclusively the diffusion term of a differential equation. In the incompressible unsteady Navier–Stokes Eq. (1), this term reads in cylindrical coordinates

$$\nu \nabla^2 \vec{u} = \nu \Delta \vec{u} - \frac{\nu}{r^2} \begin{bmatrix} 0 \\ v + 2\partial_\varphi w \\ w - 2\partial_\varphi v \end{bmatrix}, \tag{14}$$

where

$$\Delta \equiv \partial_z \partial_z + \frac{1}{r} \partial_r r \partial_r + \frac{1}{r^2} \partial_\varphi \partial_\varphi \tag{15}$$

and $\vec{u} = (u, v, w)^{\mathrm{T}}$ are the velocity components in axial, radial and azimuthal direction (z, r, φ), respectively. After Fourier discretization in the azimuthal direction, diagonalization with mapped variables $\tilde{v}_k = \hat{v}_k + \mathrm{i}\hat{w}_k$ and $\tilde{w}_k = \hat{v}_k - \mathrm{i}\hat{w}_k$ and symmetrization by multiplication with r (see [12]) we arrive at

$$\nu [r \nabla^2 \vec{u}]_k^{\sim} = \nu \begin{bmatrix} \left(\partial_z r \partial_z + \partial_r r \partial_r - \frac{k^2}{r}\right) \hat{u}_k \\ \left(\partial_z r \partial_z + \partial_r r \partial_r - \frac{(k+1)^2}{r}\right) \tilde{v}_k \\ \left(\partial_z r \partial_z + \partial_r r \partial_r - \frac{(k-1)^2}{r}\right) \tilde{w}_k \end{bmatrix} \tag{16}$$

with $-N \leqslant k \leqslant N$. As mentioned at the beginning of this section, a two-dimensional nodal spectral element method is applied in the meridional directions. Here, we restrict the derivation to one arbitrary quadrilateral spectral element Ω^e. Using several elements requires a global assembly, for example described in [13]. The expansion basis used for the meridional discretization

of $\hat{u}_k$, $\hat{v}_k$, and $\tilde{w}_k$ are tensorial products of the Lagrange cardinal functions h_i. Thus, the discretized Galerkin weak formulation of the viscosity term (16) reads

$$\nu \begin{bmatrix} \left(\boldsymbol{D}_z^T \boldsymbol{M}^e \boldsymbol{D}_z + \boldsymbol{D}_r^T \boldsymbol{M}^e \boldsymbol{D}_r - \frac{k^2}{r}\right) \hat{\boldsymbol{u}}_k \\ \left(\boldsymbol{D}_z^T \boldsymbol{M}^e \boldsymbol{D}_z + \boldsymbol{D}_r^T \boldsymbol{M}^e \boldsymbol{D}_r - \frac{(k+1)^2}{r}\right) \tilde{\boldsymbol{v}}_k \\ \left(\boldsymbol{D}_z^T \boldsymbol{M}^e \boldsymbol{D}_z + \boldsymbol{D}_r^T \boldsymbol{M}^e \boldsymbol{D}_r - \frac{(k-1)^2}{r}\right) \tilde{\boldsymbol{w}}_k \end{bmatrix}, \tag{17}$$

where the matrices $\boldsymbol{D}_z$ and $\boldsymbol{D}_r$ represent the derivatives of the basis functions in axial and radial directions. The diagonal mass matrix $\boldsymbol{M}^e$ contains the quadrature weights multiplied by the radius and the Jacobian of the mapping from the arbitrary element Ω^e to the two-dimensional standard element $\Omega^s = [-1,1] \times [-1,1]$. Finally, the entries in $\hat{\boldsymbol{u}}_k$, $\tilde{\boldsymbol{v}}_k$, and $\tilde{\boldsymbol{w}}_k$ represent the coefficients of $\hat{u}_k$, $\tilde{v}_k$, and $\tilde{w}_k$ at the quadrature points. For further details we refer to [12 and 13].

Following [4,8] we now employ a diagonal SVV tensor, where each coordinate direction is provided with its own intensity and its own kernel. Since diagonalization and symmetrization are linear operations, SVV stabilization can be introduced directly in (17). Thus, the SVV-enhanced diffusion term reads

$$\nu \begin{bmatrix} \left((\boldsymbol{D}_z^{\mathrm{svv}})^T \boldsymbol{M}^e \boldsymbol{D}_z^{\mathrm{svv}} + (\boldsymbol{D}_r^{\mathrm{svv}})^T \boldsymbol{M}^e \boldsymbol{D}_r^{\mathrm{svv}} - \frac{k^2}{r}\left(1 + \frac{\varepsilon_\varphi}{\nu} \widehat{\mathrm{Q}}_{\varphi,k}\right)\right) \hat{\boldsymbol{u}}_k \\ \left((\boldsymbol{D}_z^{\mathrm{svv}})^T \boldsymbol{M}^e \boldsymbol{D}_z^{\mathrm{svv}} + (\boldsymbol{D}_r^{\mathrm{svv}})^T \boldsymbol{M}^e \boldsymbol{D}_r^{\mathrm{svv}} - \frac{(k+1)^2}{r}\left(1 + \frac{\varepsilon_\varphi}{\nu} \widehat{\mathrm{Q}}_{\varphi,k}\right)\right) \tilde{\boldsymbol{v}}_k \\ \left((\boldsymbol{D}_z^{\mathrm{svv}})^T \boldsymbol{M}^e \boldsymbol{D}_z^{\mathrm{svv}} + (\boldsymbol{D}_r^{\mathrm{svv}})^T \boldsymbol{M}^e \boldsymbol{D}_r^{\mathrm{svv}} - \frac{(k-1)^2}{r}\left(1 + \frac{\varepsilon_\varphi}{\nu} \widehat{\mathrm{Q}}_{\varphi,k}\right)\right) \tilde{\boldsymbol{w}}_k \end{bmatrix}. \tag{18}$$

Here, $\widehat{\mathrm{Q}}_{\varphi,k}$ realizes the spectral damping in azimuthal direction and the superscript svv of the both differentiation matrices $\boldsymbol{D}_z$ and $\boldsymbol{D}_r$ indicates their modification in the following way: Owing to the use of quadrilateral elements, the tensorial structure of the expansion basis can be exploited for an efficient evaluation of the derivatives, which can be expressed as a series of the one-dimensional operations. In particular, the differentiation matrices for a two-dimensional domain can be constructed using the GLL differentiation matrix of the one-dimensional standard domain, which can be augmented by SVV as shown in (13). Since we always use the same polynomial order in both spectral element directions, an identical SVV parameterization is applied in the axial and the radial direction. Therefore, only two parameters control the spectral vanishing viscosity in the spectral element planes, which we call henceforth M_{zr} and ε_{zr}. Accordingly, the SVV parameters in Fourier direction are called M_φ and ε_φ.

2.3. Kernel modifications in azimuthal Fourier direction

At this point it should be noted that in Cartesian coordinates each wave number k is associated with a unique wave length, which is given by $\lambda = 2\pi L/k$, where L represents a geometric length scale. Hence, waves of length λ are uniformly damped according to the spectral viscosity $\varepsilon\widehat{\mathrm{Q}}(k)$. In cylindrical coordinates, this relation is still valid for the radial and axial directions. For the azimuthal direction, however, the wave length is given by $\lambda = 2\pi r/k$, i.e. for a fixed wave number the length varies linearly with the radial position. Consequently, the effect of the azimuthal spectral viscosity $\varepsilon_\varphi \widehat{\mathrm{Q}}_\varphi(k)$ to the fluid flow depends on the radial position. To clarify this we introduce $\widehat{\mathrm{Q}}_{\varphi,\lambda}$ with

$$\widehat{\mathrm{Q}}_{\varphi,\lambda} = \widehat{\mathrm{Q}}_\varphi(k(\lambda, r)) = \widehat{\mathrm{Q}}_\varphi\left(\frac{2\pi r}{\lambda}\right). \tag{19}$$

Since only the ratio of λ and r is required, (19) is equivalent to

$$\widehat{\mathrm{Q}}_{\varphi,\lambda} = \widehat{\mathrm{Q}}_\varphi\left(\frac{2\pi r^*}{\lambda^*}\right), \tag{20}$$

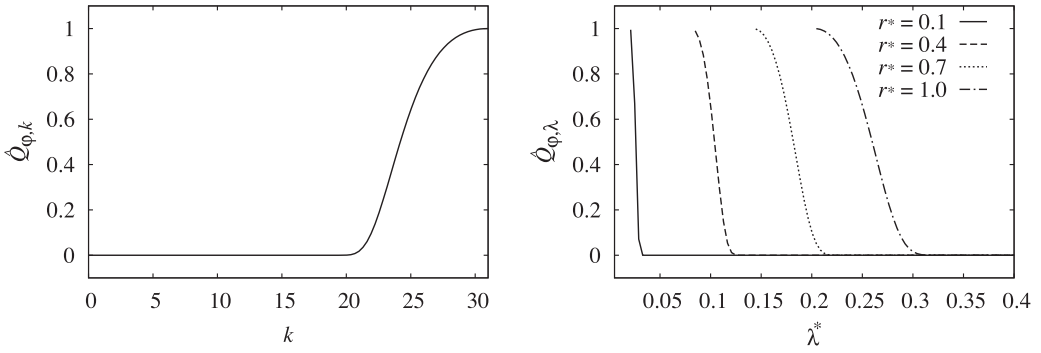

Fig. 2. Standard SVV kernel Qs as a function of wave number k and nondimensional wave length λ^* with $N = 31$, $M = 16$.

with nondimensional wave length $\lambda^* = \lambda/R$ and radius $r^* = r/R$, where R is any reference radius. In the present work, the maximum radius of the spatial domain is always chosen as reference. For the standard kernel, which is referred to as Qs in the following, Fig. 2 shows a comparison of the $\widehat{Q}_{\varphi,k}$ and $\widehat{Q}_{\varphi,\lambda}$ for $N = 31$ and $M = 16$. Clearly the threshold wave length $\lambda^*_M = 2\pi r^*/M$, above which $\widehat{Q}_{\varphi,\lambda}$ vanishes, becomes infinitely small for r approaching zero. Since the corresponding r and z scales are virtually independent from the radial position, the SVV operator becomes strongly anisotropic near the axis. Formally, this property reflects the anisotropy of the numerical grid in a consistent manner. However, due to the nonlinear nature of the underlying equations, processes at different length scales and coordinate directions are coupled to each other. For example one can imagine a fine elongated structure that is aligned with the axis and initially resolved, but becomes unrepresentable on the grid as a consequence of being tilted into another direction. This effect could induce an accumulation of small structures near the axis and, indeed such behaviour appeared in our studies and will be detailed below.

A promising approach to avoid the described mechanism is to filter out length scales that are not uniformly resolved (i.e. below the resolution limit of the radial and axial directions). Within the SVV framework, a natural realization of this concept is to mitigate the anisotropy of the SVV operator by modifying the azimuthal kernel in order to restore its stabilizing function in the axis region. From a physical point of view this suggests that waves of equal length experience the same attenuation independent from their radial position. However, this superficially attractive feature is accompanied by the presence near the axis of steep gradients in wave number space, which would destroy the spectral convergence of the overall approach. Therefore, we consider as compromise the following two modifications of the azimuthal SVV kernel, which are both smooth in wave number space:

- Qm1: Radial scaling of the spectral viscosity activation mode M.

$$\widehat{Q}^{\mathrm{m1}}_{\varphi,k} = \exp\left(-\frac{(N-k)^2}{(Mr^*-k)^2}\right) \tag{21}$$

for $M\,r^* \leqslant k \leqslant N$. Here, the nondimensional radius r^* is used, because N, M and k are integer values and possess no dimension.

- Qm2: Radial shifting of the shape function.

$$\widehat{Q}^{\mathrm{m2}}_{\varphi,k} = \exp\left(-\frac{(N-M(1-r^*)-k)^2}{(Mr^*-k)^2}\right) \tag{22}$$

for $M\,r^* \leqslant k \leqslant N - M(1-r^*)$ and $\widehat{Q}^{(2)}_{\varphi,k} = 1$ for $k > N - M(1-r^*)$.

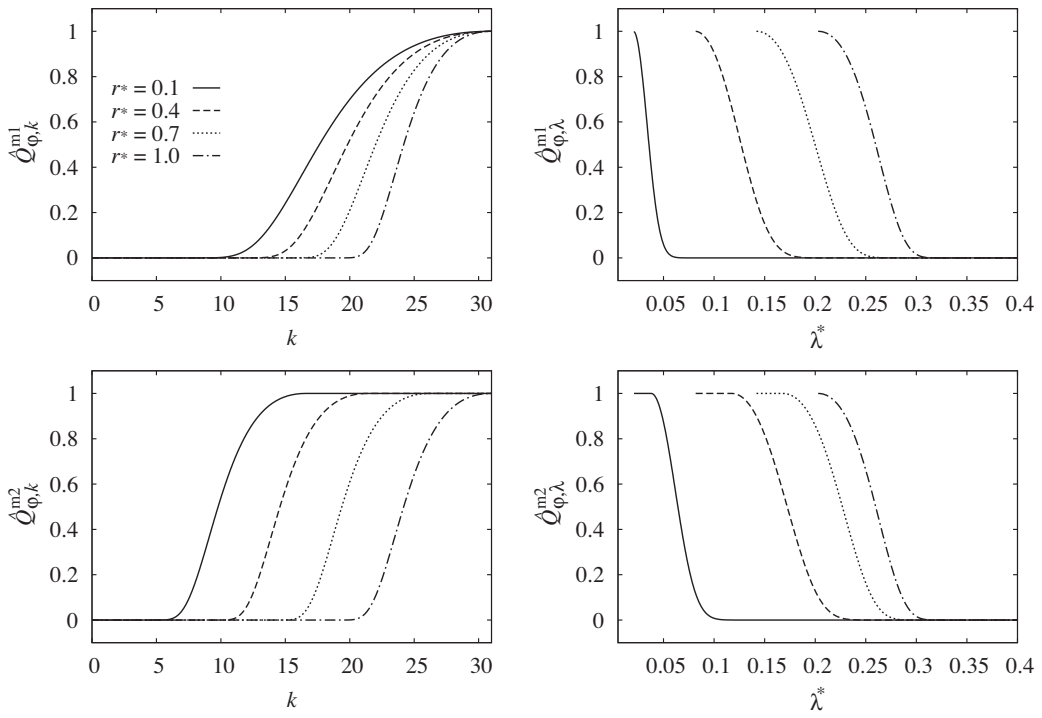

Fig. 3. Modified SVV kernels Qm1 and Qm2 as functions of wave number k or nondimensional wave length λ^* with $N = 31$, $M = 16$.

Fig. 3 shows the modified kernels as a function of wave number k and wave length λ. In comparison to the standard kernel Qs, the modifications Qm1 and Qm2 introduce an enhancement of the spectral viscosity near the axis in comparison to the standard kernel Qs. However, in both cases the viscosity still disappears for any finite wave length if r goes to zero.

In the following sections we present three incompressible flow problems to highlight different aspects of SVV in cylindrical configurations and influence of the above described kernel modifications: a three-dimensional laminar flow to study the convergence properties of the SVV kernels, turbulent pipe flow, which is a classical test case to examine LES configurations in cylindrical coordinates, and, finally, a turbulent flow in a closed cavity driven by an electromagnetic volume force.

3. Convergence study

To verify the spatial convergence properties of the SVV kernels we consider the (steady) Kovasznay flow. Originally defined for two-dimensional Cartesian coordinates [15], the exact solution of this flow can be adopted as a test case for cylindrical coordinates [12] using

$$\begin{aligned} u &= 1 - \exp(\lambda z)\cos(2\pi[r\cos(\varphi+\theta)+\Delta]),\\ v &= \frac{1}{2\pi}\lambda\exp(\lambda z)\sin(2\pi[r\cos(\varphi+\theta)+\Delta])\cos(\varphi+\theta),\\ w &= -\frac{1}{2\pi}\lambda\exp(\lambda z)\sin(2\pi[r\cos(\varphi+\theta)+\Delta])\sin(\varphi+\theta),\\ p &= \frac{1}{2}(1-\exp(\lambda z)), \end{aligned} \tag{23}$$

where $\lambda = \mathrm{Re}/2 - \sqrt{\mathrm{Re}/4^2 + 4\pi^2}$ with the Reynolds number Re. The introduction of the parameters Δ and θ enables an arbitrary offset and an arbitrary rotation about the cylinder axis, as illustrated in Fig. 4. An offset $\Delta \neq 0$ leads to a flow that crosses the axis and a rotation θ, which is a non-rotational multiple of π, ensures that both the real and the imaginary parts of all modes are exercised.

For the convergence tests, similar to those of [12] but here with SVV kernels also included, we use $\Delta = 0.1$, $\theta = 0.75$ and Reynolds number Re = 40. The computational domain is divided into $2(N+1)$ meridional semi-planes corresponding to the complex Fourier modes. Each semi-plane is discretized with a non-orthogonal grid consisting of seven spectral elements; Fig. 5 shows the spectral element grid and the internal mesh nodes for polynomial order $P = 6$. Furthermore, Dirichlet boundary conditions are applied on all exterior (non-axial) domain nodes. For each interpolation order (P,N), the exact velocity field is supplied as initial condition. The problem is then integrated forwards in time to steady state. Finally, the error is determined by computing the maximum deviation of the steady state from the exact solution. Here, the axial velocity u component is used as reference; the other two components behave similarly.

We have performed two different studies in order to investigate the convergence properties of the SVV stabilization separately for the spectral element method and the Fourier method. In the first, we have validated the SVV implementation in the meridional directions: the polynomial order of the spectral elements is varied between $P = 2$ and $P = 18$, while a constant number of Fourier modes, namely $N = 24$, is maintained in azimuthal direction. This ensures that the error is dominated by the spectral element discretization at low P, while the azimuthal direction is fully resolved. Fig. 6 (a) shows error plotted against P both with and without SVV. As demonstrated by previous authors, SVV somewhat reduces the rate of convergence, but exponential/spectral convergence is preserved. SVV parameters are computed as in [4] as follows: $M_{zr} = P/2$ and $\varepsilon_{zr} = 1/P$. Alternative parameterizations, e.g. with $M_{zr} = 2\sqrt{P+1}$ and $\varepsilon_{zr} = 1/(P+1)$ as in [7], gave similar results.

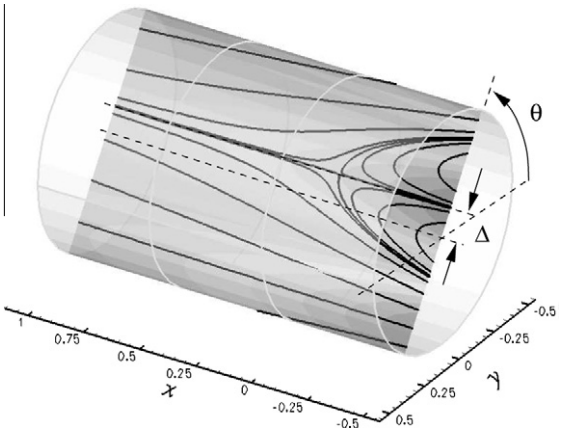

Fig. 4. Streamlines of the cylindrical Kovasznay flow for Re = 40.

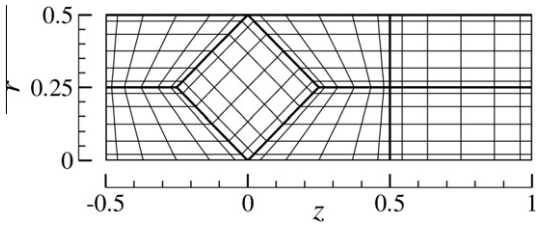

Fig. 5. Spectral element mesh adopted for the meridional semi-plane in convergence testing with Kovasznay flow, showing collocation points for $P = 6$.

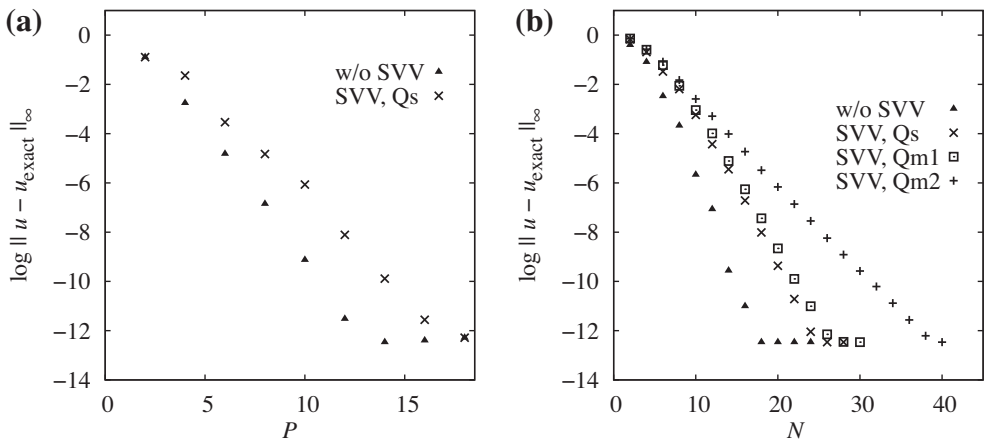

Fig. 6. Convergence results for Kovasznay flow with or without using SVV. In azimuthal direction the kernel versions Qs, Qm1 and Qm2 are tested. In (a), the polynomial order P of the spectral elements varies while azimuthal resolution is kept constant, with $N = 24$. In (b) the number of Fourier modes N increases for fixed spectral element shape function order $P = 14$.

In the second study, a fixed spectral element polynomial order $P = 14$ is used, and the number of azimuthal Fourier modes is varied. We have examined the standard SVV kernel Qs and its variations Qm1 and Qm2, which were introduced in the previous section. The SVV parameters are scaled as above, i.e. $M_\varphi = N/2$ and $\varepsilon_\varphi = 1/N$. Fig. 6 (b) presents a summary of these results: the standard kernel Qs behaves as for the previous study where P was varied, i.e. the adoption of SVV with this kernel reduces the rate of convergence, but convergence remains exponential. In comparison to Qs, the modified kernels further reduce the convergence rate. This can be explained by the fact that in these cases the number of stabilized modes increases with decreasing radial position. Thus, the overall effect of SVV is stronger than in the standard case. When Qm1 is applied, this effect is marginal, because $\widehat{Q}^{\mathrm{m1}}_{\varphi,i}$ is similar to $\widehat{Q}_{\varphi,i}$ even for small radii, as illustrated in Figs. 2 and 3 of the previous section. The second variation, Qm2, also achieves spectral convergence, but at a significantly lower rate. This is not surprising when we consider that Qm2 introduces considerably more diffusion in the core region.

4. Turbulent pipe flow

The second example deals with turbulent pipe flow at Reynolds number $\mathrm{Re} = U_{\mathrm{bulk}} D/\nu = 10{,}000$. We wish to assess whether the SVV technique enables stable LES in cylindrical configurations that include the axis, and which aspects are relevant to obtaining reliable results. For all simulations we consider a pipe with diameter $D = 2R = 1$ and length $L = 2\pi D$, which is adequate at this Reynolds number [16]. No-slip boundary conditions are imposed at the wall while periodicity is employed in the streamwise direction. Our assessment is based on first and second-order statistics. DNS data serves as reference, which we first validate using experimental data.

4.1. Comparison of DNS and experimental data

The DNS grid consists of 320 semi-planes (i.e. $N = 159$) in the azimuth and 30×8 spectral elements with $P = 10$ in the axial and the radial direction (Fig. 7). When designing the mesh, we have employed rules of thumb for for near-wall resolution in DNS supplied by Piomelli [17]. We have retained a strategy which has been found successful in previous spectral-element-based DNS and wall-resolving LES [14,16]: the first element covers the laminar sublayer and another one the buffer layer, where turbulent energy production is greatest. A geometric progression with a stretching factor of 1.2 is then used to reach the centre of the pipe.

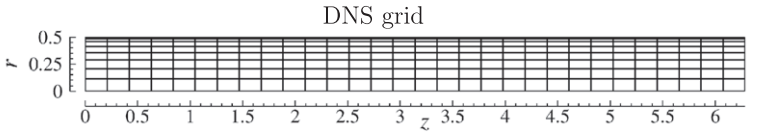

Fig. 7. Spectral element boundaries for DNS of turbulent pipe flow.

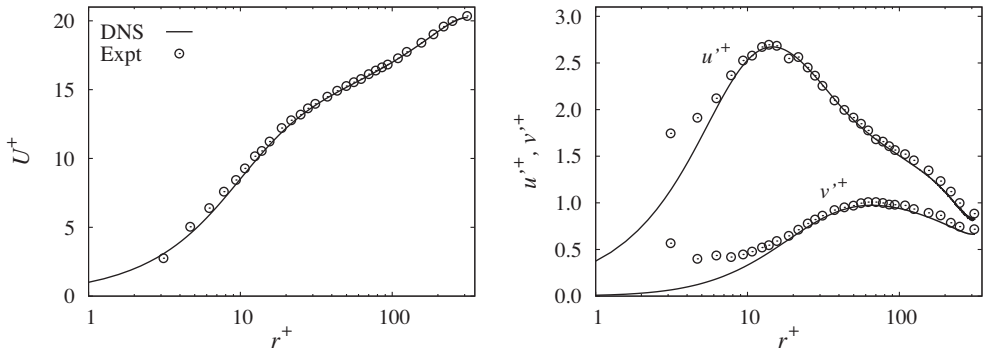

Fig. 8. DNS and experimental data for turbulent pipe flow, Re = 10 000. Comparison of mean flow (left) and rms (u'^+, stream-wise; v'^+, wall-normal) velocity fluctuation profiles (right) resulting from simulation and LDA measurements [18].

In order to help build confidence in the veracity of the DNS results, we compare the mean flow and the fluctuations in stream-wise (axial) and wall-normal (radial) direction with experimental data from den Toonder and Nieuwstadt [18] who carried out laser Doppler anemometer (LDA) measurements in a recirculatory pipe flow facility. Fig. 8 presents the time-averaged streamwise velocity U and the rms values u' and v' of the axial and radial velocity fluctuations in viscous units, i.e. the velocity components are scaled with the wall friction velocity u_τ: $U^+ = U/u_\tau$, $u'^+ = u'/u_\tau$ and $v'^+ = v'/u_\tau$. The corresponding coordinate in wall-normal direction is given by $r^+ = (R - r)u_\tau/\nu$. Generally, the computed results are in good agreement with the experimental results, and with similar DNS results presented in [16]. We note that the experimental data for rms values seem unreliable close to the wall.

4.2. Construction of LES grids

To generate a wall-resolving LES grid, the DNS grid is coarsened approximately by a factor of three in each direction: In the azimuth 96 semi-planes ($N = 47$) are used. The domain is divided into 10 spectral elements in the streamwise direction. The discretization in the radial direction was not so straightforward as for the other two directions, since this direction has been discretized using only three elements. We have proceeded as follows: the size of the element at the wall is trebled compared to the DNS, giving a near-wall wall-normal resolution of $r^+ \approx 0.9$, sufficient to capture the viscous sublayer. The remaining space is occupied by two elements with a stretching factor of 1.5. In summary, the element extents in the wall-normal direction, starting from the wall, are $\Delta r_1 = 0.045$, $\Delta r_2 = 0.182$ and $\Delta r_3 = 0.273$. Fig. 9 shows the resulting spectral element grid 1. The polynomial order in the axial and the radial direction was retained from the DNS, i.e. $P = 10$. Further, the size of the time step could be doubled so that the overall computational cost for the LES was approximately 0.5% that of the DNS.[1] In order to study the influence of radial grid refinement we further introduce two variations. In the first case, grid 2, the radial size of the two inner layers of elements is changed to $\Delta r_2 = \Delta r_3 = 0.2225$. For the second variation, grid 3, the axis elements of the original grid are divided into two elements, where the size of the innermost layer corresponds to the DNS resolution at the axis such that $\Delta r_3 = 0.160$ and $\Delta r_4 = 0.113$. Other grid parameters remained unchanged.

4.3. SVV parameter study using the standard kernel Qs

First we examine the influence of SVV parameters when the standard kernel Qs is applied. Starting with the spectral viscosity activation modes $M_{zr} = P/2 = 5$ and $M_\varphi = (N + 1)/2 = 24$, the SVV amplitudes ε_{zr} and ε_φ were increased independently from 3ν to 20ν. Notice that the amplitudes must scale with ν for dimensional reasons. The dependence from P and N respectively is not explicitly indicated, because these parameters were not modified. Fig. 10 illustrates the outcome of this variation for $\varepsilon_{zr} = \varepsilon_\varphi = 5\nu$, 10ν, and 20ν. For smaller amplitudes the simulations were unstable. One observes that the LES results are generally in very good agreement with the DNS reference data. Moreover, the mean flow as well as the rms profiles are

[1] Simulations were performed on a SGI Altix 4700 at ZIH/TU Dresden.

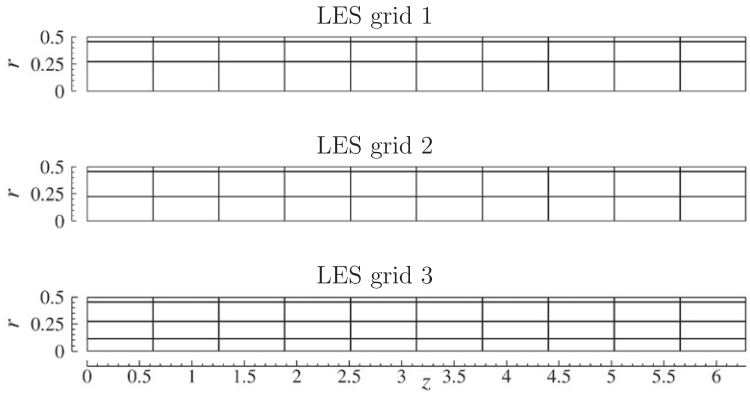

Fig. 9. Spectral element boundaries for LES of turbulent pipe flow.

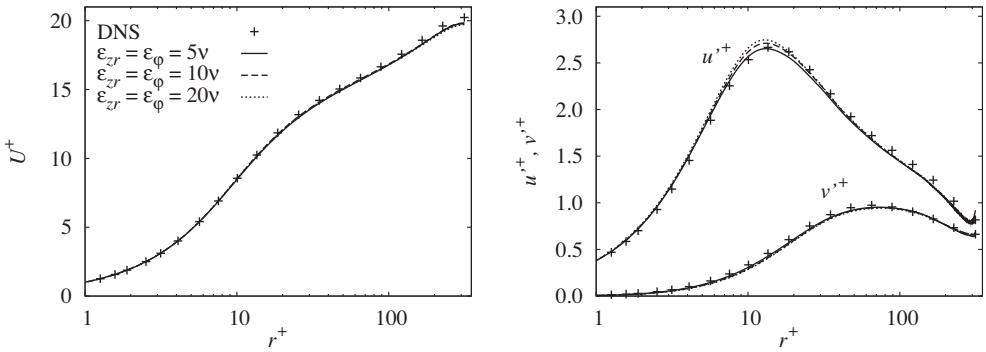

Fig. 10. Mean flow (left) and rms velocity fluctuation profiles (right) for turbulent pipe flow, when ε_{zr} and ε_{φ} are varied and LES grid 1 is used. In all three spatial direction the standard SVV kernel Qs is applied. The spectral viscosity activation wave numbers are held constant at ($M_{zr} = 5$, $M_{\varphi} = 24$) and the DNS results serve as reference.

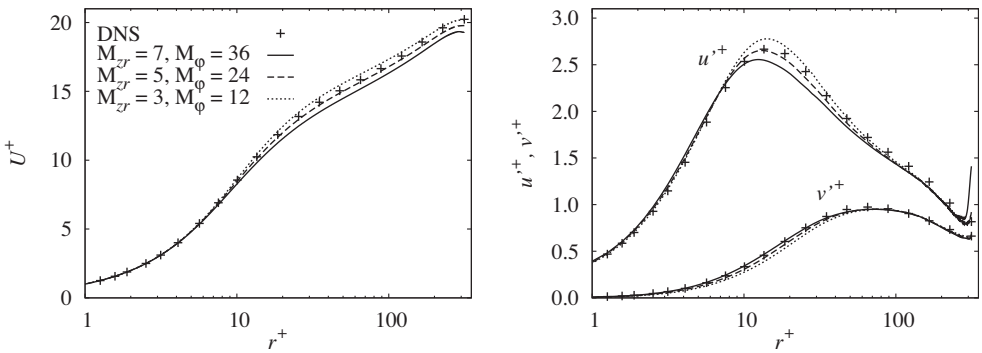

Fig. 11. Mean flow (left) and rms velocity fluctuation profiles (right) for turbulent pipe flow at various activation wave numbers M_{zr} and M_{φ} using LES grid 1 and SVV kernel Qs with $\varepsilon_{zr} = \varepsilon_{\varphi} = 5\nu$.

almost unaffected by the parameter variation. Only the streamwise fluctuations increase slightly for higher amplitudes. The best agreement is received with the smallest stable amplitude, namely $\varepsilon_{zr} = \varepsilon_{\varphi} = 5\nu$.

Subsequently, the activation wave numbers M_{zr} and M_{φ} were varied, with fixed SVV amplitudes $\varepsilon_{zr} = \varepsilon_{\varphi} = 5\nu$. These results are presented in Fig. 11. Here, the effect of parameter variation is more evident. With increasing activation wave numbers, the mean flow and the wall-normal fluctuations profiles agree somewhat better with the reference data, whereas the streamwise fluctuations profiles get closest to the reference curve for $M_{zr} = 5$ and $M_{\varphi} = 24$. However we note here that the parameter combination $M_{zr} = 7$ and $M_{\varphi} = 36$ showed first signs of numerical instability in terms of temporarily increasing divergence energy of the velocity field. Therefore, the 'optimal' parameter configuration for this test case was provided by

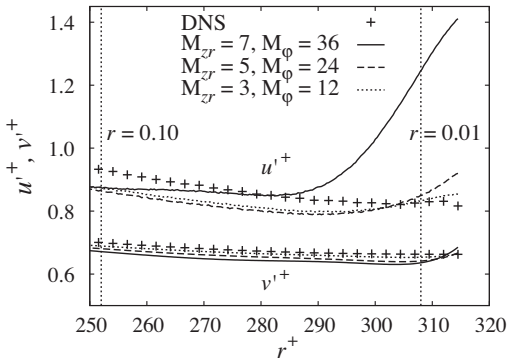

Fig. 12. Details of the near-axis rms velocity fluctuation profiles for turbulent pipe flow (cf. Fig. 11), for various activation wave numbers (cf. Fig. 11). Radial positions $r = 0.01$ and 0.10 are marked and will be referred to in discussion for Fig. 13.

$$M_{zr} = 5, \quad M_\varphi = 24, \quad \text{and} \quad \varepsilon_{zr} = \varepsilon_\varphi = 5\nu. \tag{24}$$

We are aware that the present parameter study is not universally valid, but a trend is apparent: the best results were obtained for high activation modes and small SVV amplitudes, as long as these parameters ensured a stable calculation. Similar observations were made in previous SVV studies (see e.g. [5]).

4.4. Near-axis behaviour

When we take a closer look at developments near the pipe axis (see Fig. 12) a non-physical increase of fluctuation becomes evident in this region, especially for high activation wave numbers. A possible explanation for this is given by the mutual disappearance of SVV stabilization with decreasing radius, allowing small-scale structures to accumulate in the core region. To investigate this effect in more detail, azimuthal wave number spectra for various radii were computed for the DNS as well as the LES calculations. The azimuthal spectra were determined by first computing the kinetic energy of Fourier transformed, instantaneous velocity fields. These instantaneous fields were averaged in axial direction, followed by an averaging in time, for which up to 40 independent snapshots were used. Finally, local spectra were extracted at different radial positions.

Fig. 13 presents a comparison between DNS and LES spectra for $r = 0.01$, 0.1, 0.25 and 0.45, corresponding to 2%, 20%, 50% and 90% of R, respectively. At the outer two radial positions, the DNS and LES spectra agree well with each other. The stronger decay of the LES spectrum for modes $k \gtrsim 30$ is attributed to the augmented viscosity on these modes. In case of $r = 0.1$, this effect of SVV is still apparent. However, in comparison to DNS, a higher energy level is observed at higher wave numbers. In the lower range, $k \lesssim 10$, the correspondence of both spectra is still good. In contrast, at the smallest radial position $r = 0.01$, the energy level of the LES is approximately one order of magnitude larger than the DNS results at all wave numbers. This observation suggests that there may be insufficient dissipation of turbulent kinetic energy in the centre of the pipe. At this point it is worth noting that the azimuthal wave length of the largest structures near the axis, e.g.

$$\lambda_{\max}(r = 0.01) = \frac{2\pi r}{1} = \frac{\pi}{50},$$

approximately corresponds to the smallest resolved scales in the outer region

$$\lambda_{\min}(r = R) = \frac{2\pi R}{N} = \frac{\pi}{47}.$$

This implies that turbulent structures transported from the outer regions to the centre are not adequately dissipated and hence appear to accumulate in the core region.

4.5. Influence of kernel modification in azimuthal direction

Next we consider the modified azimuthal kernels Qm1 and Qm2. We have again chosen the parameter set according to (24). Generally, the results are almost identical to those obtained with Qs. In particular, neither Qm1 nor Qm2 manage to diminish the overshoot of turbulent kinetic energy near the axis as displayed in Fig. 14. Closer examination of the azimuthal spectra for Qm2 reveals an improvement for smaller radii such as $r = 0.1$ (Fig. 15). However, in the immediate vicinity of the axis, at $r = 0.01$, kernel Qm2 (as well as Qm1) fails to control an accumulation of energy at low wave numbers. As argued above, for small radii all azimuthal modes correspond to small length scales. On the other hand, those scales cannot be represented in the spectral element directions (z, r), whose discretization is relatively coarse at the axis. Hence, one may presume that the nonlinear redistribution of energy between the different coordinate directions and corresponding velocity

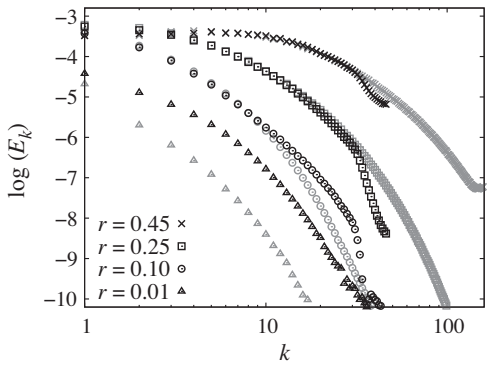

Fig. 13. Averaged kinetic energy in non-axisymmetric modes in turbulent pipe flow for different radii, as functions of azimuthal wave number k. DNS results are displayed in grey, with corresponding LES results in black. SVV parameters for the LES are $M_{zr} = 5$, $M_\varphi = 24$ and $\varepsilon_{zr} = \varepsilon_\varphi = 5\nu$. LES grid 1 and kernel Qs is used.

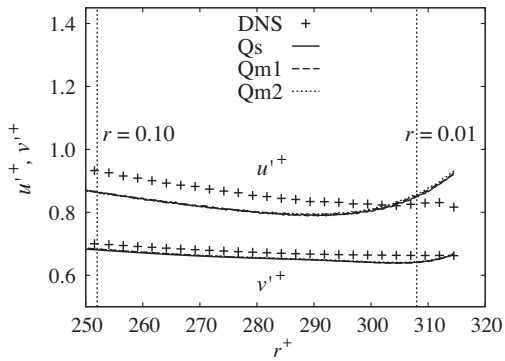

Fig. 14. Mean flow and rms velocity fluctuations near the axis, when kernels Qs, Qm1 or Qm2 are applied in the azimuth. (In axial and radial directions Qs is applied.) SVV parameters are $M_{zr} = 5$, $M_\varphi = 24$ and $\varepsilon_{zr} = \varepsilon_\varphi = 5\nu$. LES grid 1 is used.

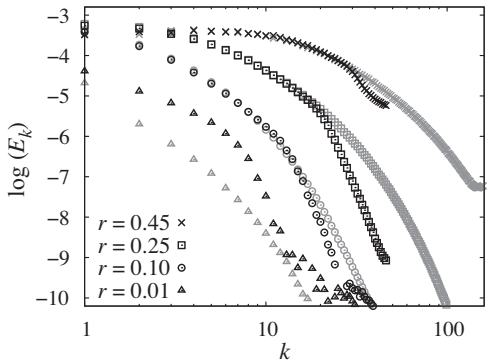

Fig. 15. Averaged kinetic energy spectra using kernel Qm2 in the azimuth and LES grid 1. Results of the DNS are displayed in grey, with those for LES in black.

components cannot be captured properly. This suggests that a local refinement of the spectral element grid near the axis would improve redistribution.

4.6. Radial grid refinement in axis region

In order to verify this hypothesis, we have performed additional LES calculations with two further spectral element grids that are modified accordingly. An illustration of all three grids were given in Fig. 9. In contrast to grid 1, the radial size of the two inner layers of elements is equal in grid 2 and for grid 3 an additional element layer is introduced at the axis.

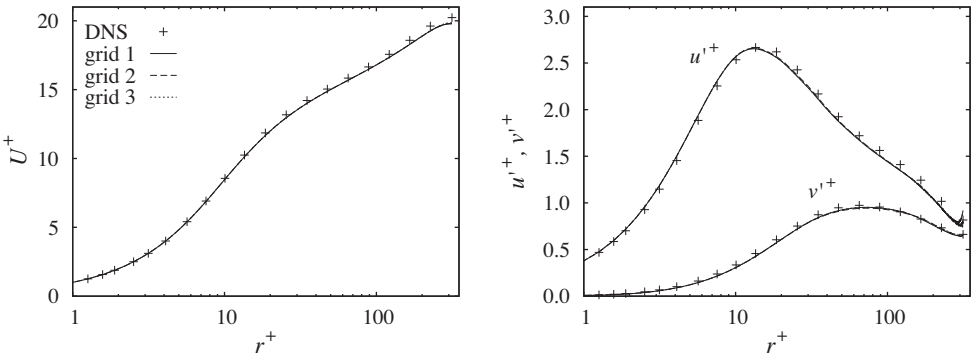

Fig. 16. Mean flow (left) and rms velocity fluctuation profiles (right) for various grids used for turbulent pipe flow. For LES, the standard kernel Qs is used in all spatial directions, with parameters $M_{zr} = 5, M_\varphi = 24$ and $\varepsilon_{zr} = \varepsilon_\varphi = 5\nu$. The LES results for the different grids are indistinguishable except in the near-axis region (see Fig. 17).

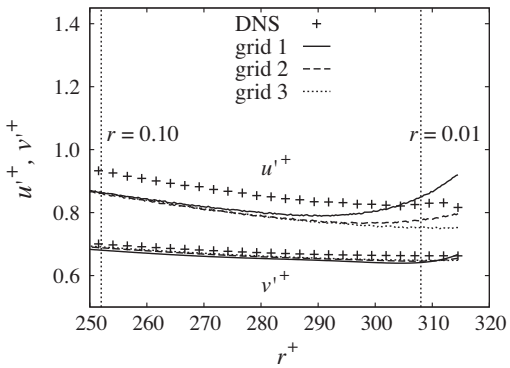

Fig. 17. Details of the rms velocity fluctuation profiles near the axis for various grids using standard SVV kernel Qs (cf. Fig. 16).

Fig. 16 presents the influence of the radial resolution on the mean flow and the rms values of axial and radial velocity fluctuations. The LES were performed with the standard kernel Qs and, as above, the SVV parameter configuration (24) is used. One initially observes that the grid modifications do not degrade the overall good agreement with the DNS data. Closer examination of the near-axis region (Fig. 17) reveals that the use of grid 2 diminishes the accumulation of turbulent kinetic energy in this region. The introduction with grid 3 of near-axis radial element resolution equivalent to that used in DNS prevents the non-physical increase of fluctuations. In order to study the influence of the local refinement in more detail, energy spectra of the latter case are displayed along with the DNS data in Fig. 18. In comparison to the results obtained with Qs and the original grid (cf. Fig. 13), the radial refinement in the core region removes the energy overshot at smaller radii $r \leqslant 0.1$. For the outer radii of the pipe, the spectra remain unchanged, since the grid modification does not affect this region. Hence, the hypothesis stated above is validated in the sense that a proper choice of the spectral element resolution is able to suppress near-axis axis instability, even though the standard SVV kernel Qs is used.

5. Flow driven by a travelling magnetic field

As third test case we consider the flow driven by a travelling magnetic field (TMF) in a closed, non-conductive cylindrical cavity with aspect ratio one, i.e. height H is twice the radius R. The body force is given by

$$\vec{f} = F\frac{\varrho\nu^2}{2R^3}\left(\frac{r}{R}\right)^2\vec{e}_z,$$

where

$$F = \frac{\sigma\omega B^2\kappa R^5}{4\varrho\nu^2}$$

is the nondimensional forcing parameter, σ is electric conductivity, ω is angular frequency, κ is axial wave number and B is the induction of the magnetic field. DNS of the resulting turbulent flow were presented in [11] for $F = 1 \times 10^6$ and 4×10^6. This corresponds approximately to $8F_c$ and $32F_c$, where $F_c = 120{,}400$ is the critical force parameter [19]. Here we use the DNS

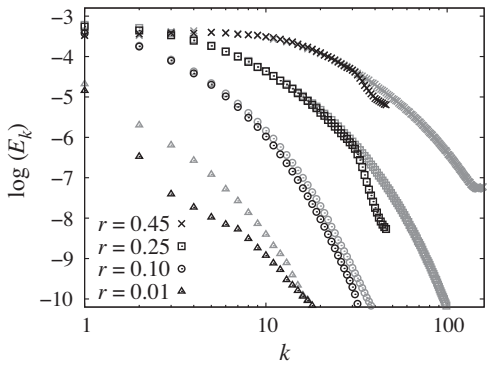

Fig. 18. Averaged kinetic energy spectra of DNS and LES using Qs and grid 3. The results of the DNS are displayed in grey and corresponding results of LES in black.

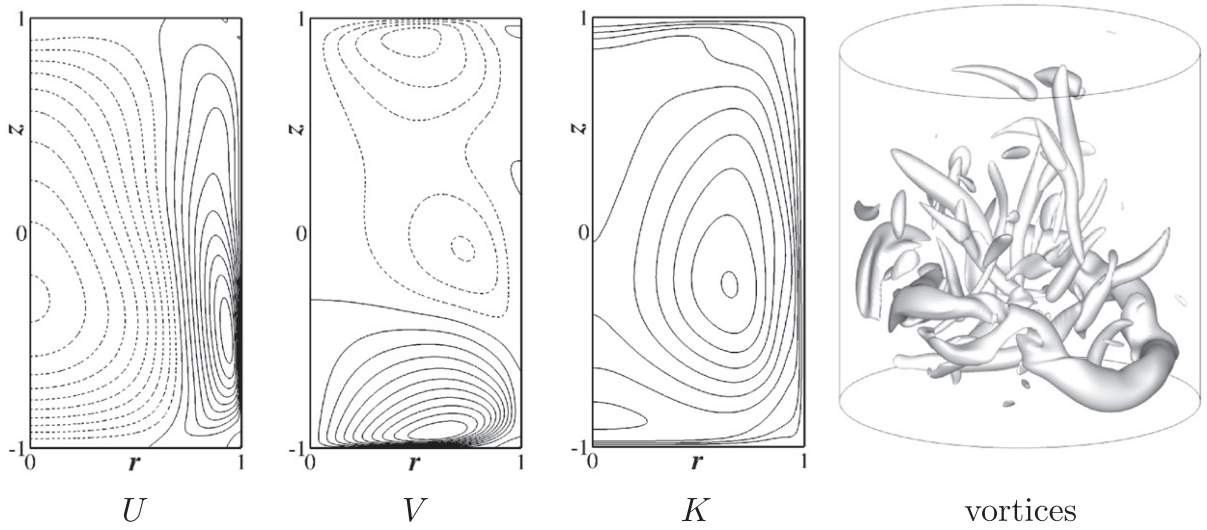

Fig. 19. DNS results for the flow induced by an eight-times supercritical travelling magnetic field (TMF). From left to right: Contours of axial mean velocity from −750 to 750 with step 75, contours of radial mean velocity from −500 to 500 with step 50, contours of turbulent kinetic energy from 0 to 110000 with 10000, and instantaneous vortices visualized with second invariant of the velocity gradient tensor ($\lambda_2 = -1.5 \times 10^7$). Dashed contour lines indicate negative values.

for $F = 1 \times 10^6$ as the reference case. Fig. 19 depicts the components of the axial and radial mean flow U and V, the distribution of turbulent kinetic energy $K = (u'^2 + v'^2 + w'^2)/2$ and a typical snapshot of the vortex structures using the λ_2-criterion according to [20]. All quantities presented in this Section have been nondimensionalized using the radius and the kinematic viscosity as primary scales such that velocity, time, and coordinates are scaled with v/R, R^2/v, and R, respectively.

As can be deduced from Fig. 19, the base flow is dominated by a toroidal roll that moves fluid upwards at the rim and returns it along the centre of the cylinder. However, due to strong fluctuations, the mean flow is of little relevance for the instantaneous picture. The vortices cover the major part of the domain and show a rather random orientation. However, the evolution over a time span reveals a preference of axial orientation in the centre, whereas azimuthal vortices tend to prevail near the rim. On average, turbulence amounts to nearly 50% of the total kinetic energy [11]. Hence, this flow provides an interesting supplemental test case in support of the results obtained for turbulent pipe flow.

5.1. Applied DNS and LES grids

The DNS and LES grids used for this study are displayed in Fig. 20. The DNS is performed on a non-equidistant rectangular grid of 25×50 elements with a polynomial degree of $P = 7$ and 256 semi-planes in the azimuth. For LES two different grids are used. Both grids have in common, that the number of semi-planes is reduced to 48 and that the meridional grid is coarsened to 5×10 spectral elements, whereas the polynomial degree is retained at the same value as for the DNS. The size of the wall-nearest axial and radial elements is increased slightly such that the viscous sublayer is captured with z^+ and $r^+ < 0.3$. The

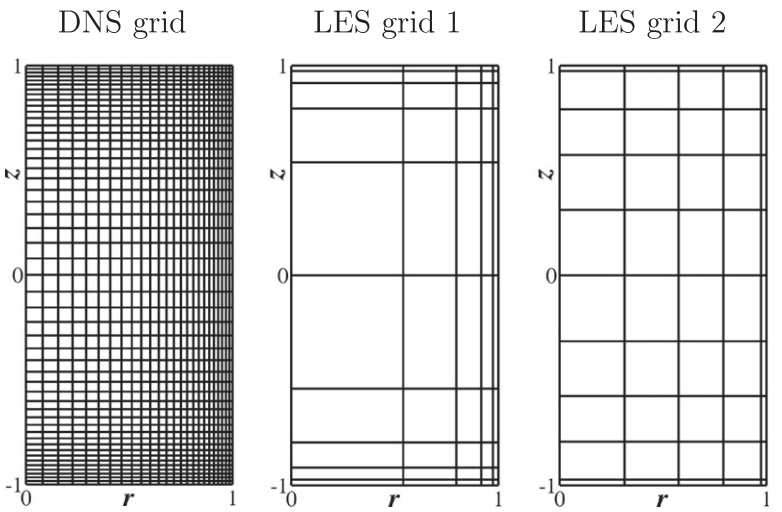

Fig. 20. Spectral element grids used for the simulations of the TMF driven flow.

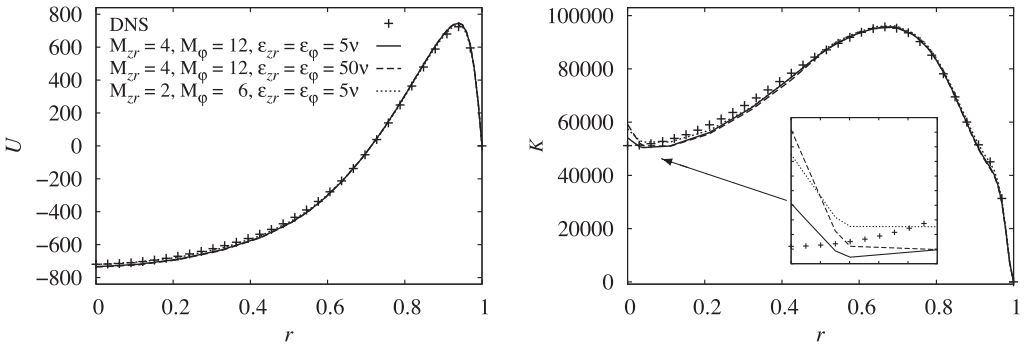

Fig. 21. Axial mean velocity (left) and turbulent energy profiles (right) $z = -0.5$ for the TMF test case using various SVV parameter combinations. Here, LES grid 1 and, in all spatial direction, SVV kernel Qs is used. DNS results of [11] serve as reference. For K, a magnification of the core region ($r \leqslant 0.1$) is displayed in the embedded diagram.

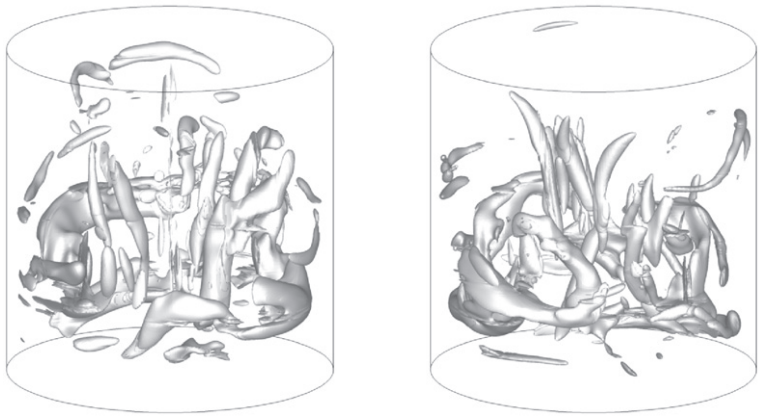

Fig. 22. Instantaneous vortex structures for the eight-times supercritical TMF driven flow computed either with LES grid 1 (left) or with LES grid 2 (right). The vortices are displayed for the same value, $\lambda_2 = -1.5 \times 10^7$, as the DNS snapshot in Fig. 19.

crucial difference between LES grids 1 and 2 lies in the near-axis radial extents of the inner spectral elements. In the first case, a constant stretching factor of 2.11 is used for all elements, including those nearest the walls. Hence, elements near the axis are extremely large. For LES grid 2, the size of the inner elements is determined independently from the outer

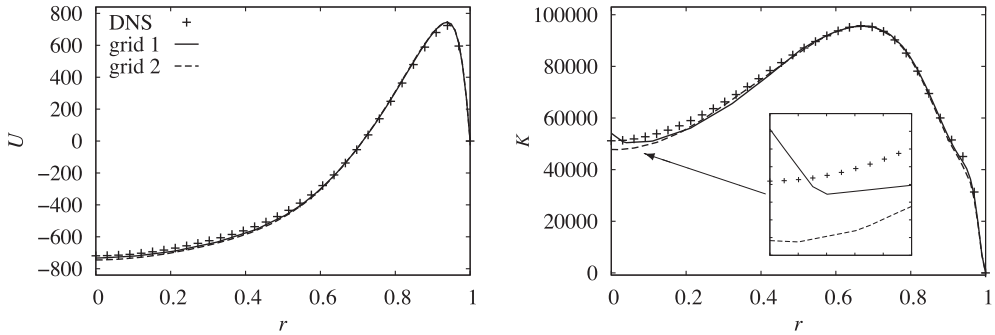

Fig. 23. Axial mean velocity (left) and turbulent energy profiles (right) $z = -0.5$ for the TMF test case using either grid 1 or grid 2. The SVV parameters are $M_{zr} = 4$, $M_\varphi = 12$, and $\varepsilon_{zr} = \varepsilon_\varphi = 5\nu$.

elements using a moderate stretching factor of 1.2 such that a higher resolution at the axis is provided. In both cases, the size of the time step is doubled. Consequently, LES costs about 0.3% of the equivalent DNS.

5.2. SVV parameter variation using the standard SVV kernel Qs

First, a parameter study was performed to investigate the influence of the SVV parameters on grid 1. Starting with a similar parameter set for the pipe flow, namely

$$M_{zr} = (P+1)/2 = 4, \quad M_\varphi = (N+1)/2 = 12, \quad \text{and} \quad \varepsilon_{zr} = \varepsilon_\varphi = 5\nu, \tag{25}$$

the SVV magnitude is increased up to 50 and, independently, the activation modes M_{zr} and M_φ are reduced to 2 and 6, respectively. Fig. 21 summarizes the outcome of this study, presenting the profiles of U and K at $z = -0.5$, where the axial mean velocity approximately reaches its maximum. At first glance, the results look very similar. As for the pipe flow outcomes, LES profiles show a remarkable agreement with the corresponding DNS data and the variation of the SVV parameters does not qualitatively change the results. Closer examination near the axis again reveals an accumulation of turbulent energy in case of LES. As illustration of these artifacts, the left side of Fig. 22 presents a snapshot of the instantaneous vortices, when grid 1 and the SVV parameter set (25) is used. One observes small vortex tubes in the core region that are aligned with the axis. These structures have no counterpart in the DNS.

5.3. Influence of SVV kernel modification or grid variation

As for the pipe flow, we have carried out simulations with the modified SVV kernels as well as with the modified LES grid (grid 2) with the aim of preventing near-axis accumulation of turbulent energy. As before, the use of Qm1 or Qm2 in azimuthal direction does not produce improvement. However, improved grid design ensures sufficient dissipation in the core region, as one may observe in Fig. 23. The vortex tubes observed in the simulation with LES grid 1 almost completely disappear when LES grid 2 is employed (see right side of Fig. 22).

6. Conclusions

The motivation for this work was to prove the capability of the spectral vanishing viscosity method for large-eddy simulations of flow problems in cylindrical coordinates that include the axis region. We first presented the principles of SVV with focus on application to a spectral-element–Fourier method for three-dimensional incompressible fluid flows. In particular, we have shown that the scales are not damped uniformly in the azimuthal direction, when the standard SVV kernel (Qs) introduced by Maday [2] is used. To mitigate this imbalance, which is seen as a possible cause of the observed near-axis instabilities, we have proposed two modifications of the standard kernel. These two variations relied on geometric considerations, where either the activation mode is down-scaled with decreasing radius or the whole shape function is shifted towards the lower modes.

To study the accuracy and stabilization of the standard SVV and its modifications, we have considered three different flow configurations. First, we examined convergence properties of all SVV kernels using the laminar Kovasznay flow. These tests revealed that the two proposed modifications Qm1 and Qm2 of the SVV kernel preserve the spectral convergence as well as the standard version Qs. Subsequently, we performed LES of turbulent pipe flow and a supercritical flow driven by a travelling magnetic field. In general, the application of SVV stabilized the simulations and provided results in good agreement with the reference data. However, an accumulation of small-scale fluctuations near the axis was detected for both test cases. Neither variation of SVV parameters nor the use of one of the remaining kernel modifications could prevent this effect. Closer

examination of azimuthal energy spectra revealed an increase of energy over the whole spectrum in the immediate vicinity of the axis independent of the SVV kernel employed. A comparison of the resolved azimuthal length scales in the outer and inner regions of the cylinder suggested that the redistribution of energy between the different spacial directions is not captured properly in the original LES grids. Hence, we have presumed that a local refinement of the spectral element grid would recover this mechanism. Indeed, proper choice of the grid prevented the accumulation of small-scale fluctuations near the axis. While such a local grid refinement helps to restore numerical stability, it is not motivated by any physical reason and, hence, should be constrained to a minimum. Our results suggest that using a nearly uniform (but possibly different) resolution for the radial and axial directions in the core region is sufficient to control the axis instability. This observation needs to be justified for other configurations. Finally, the question about the generic choice of the optimal SVV parameters still remains open and should be addressed in more detail in further research. Nevertheless, we can conclude that the spectral vanishing viscosity method is a reliable tool for the stabilization of LES when using high-order discretization methods.

Acknowledgements

The first two authors gratefully acknowledge the financial support from Deutsche Forschungsgemeinschaft in frame of the Collaborative Research Center SFB 609. Computational facilities were provided by the Center for Information Services and High Performance Computing (ZIH) of the TU Dresden. H.M.B. acknowledges support from Australia's National Computational Infrastructure through its Merit Allocation Scheme, Grant D77.

References

[1] E. Tadmor, Convergence of spectral methods for nonlinear conservation laws, SIAM J. Numer. Anal. 26 (1) (1989) 30–44.
[2] Y. Maday, S. Ould-Kaber, E. Tadmor, Legendre pseudospectral viscosity method for nonlinear conservation laws, SIAM J. Numer. Anal. 30 (1993) 321–342.
[3] G.-S. Karamanos, G.E. Karniadakis, A spectral vanishing viscosity method for large-eddy simulations, J. Comput. Phys. 163 (1) (2000) 22–50.
[4] C.J. Xu, R. Pasquetti, Stabilized spectral element computations of high Reynolds number incompressible flows, J. Comput. Phys. 196 (2) (2004) 680–704.
[5] R. Pasquetti, Spectral vanishing viscosity method for LES: sensitivity to the SVV control parameters, J. Turb. 6 (12) (2005).
[6] R. Pasquetti, Spectral vanishing viscosity method for large-eddy simulation of turbulent flows, J. Sci. Comput. 27 (1–3) (2006) 365–375.
[7] R.M. Kirby, S.J. Sherwin, Stabilisation of spectral/*hp* element methods through spectral vanishing viscosity: application to fluid mechanics modelling, Comput. Methods Appl. Mech. Eng. 195 (23–24) (2006) 3128–3144.
[8] E. Séverac, E. Serre, A spectral vanishing viscosity for the LES of turbulent flows within rotating cavities, J. Comput. Phys. 226 (2007) 1234–1255.
[9] R. Pasquetti, E. Séverac, E. Serre, P. Bontoux, M. Schäfer, From stratified wakes to rotor-stator flows by an SVV-LES method, Theoret. Comput. Fluid Dyn. 22 (3–4) (2008) 261–273.
[10] S. Poncet, E. Serre, High-order LES of turbulent heat transfer in a rotor-stator cavity, Int. J. Heat Fluid Flow 30 (4) (2009) 590–601.
[11] J. Stiller, K. Koal, A numerical study of the turbulent flow driven by rotating and travelling magnetic fields in a cylindrical cavity, J. Turb. 10 (44) (2009) 1–16.
[12] H.M. Blackburn, S.J. Sherwin, Formulation of a Galerkin spectral element–Fourier method for three-dimensional incompressible flows in cylindrical geometries, J. Comput. Phys. 197 (2004) 759–778.
[13] G.E. Karniadakis, S.J. Sherwin, Spectral/*hp* Element Method for Computational Fluid Dynamics, second ed., Numerical Mathematics and Scientific Computation, Oxford University Press, 2005.
[14] H.M. Blackburn, S. Schmidt, Spectral element filtering techniques for large eddy simulation with dynamic estimation, J. Comput. Phys. 186 (2003) 610–629.
[15] L.I.G. Kovasznay, Laminar flow behind a two-dimensional grid, Math. Proc. Camb. Philos. Soc. 44 (1948) 58–62.
[16] C. Chin, A.S.H. Ooi, I. Marusic, H.M. Blackburn, The influence of pipe length on turbulence statistics computed from direct numerical simulation data, Phys. Fluids 22 (2010) 115107-1–115107-10.
[17] U. Piomelli, Large-eddy simulations: where we stand, in: C. Liu, Z. Liu (Eds.), Advances in DNS/LES, AFOSR, Louisiana, Greyden Press, 1997, pp. 93–104.
[18] J.M.J. den Toonder, F.T.M. Nieuwstadt, Reynolds number effects in a turbulent pipe flow for low to moderate *Re*, Phys. Fluids 9 (1997) 3398.
[19] I. Grants, G. Gerbeth, Stability of melt flow due to a traveling magnetic field in a closed ampoule, J. Cryst. Growth 269 (2004) 630–638.
[20] J. Jeong, F. Hussain, On the identification of a vortex, J. Fluid Mech. 285 (1995) 69–94.